applied sciences

MDPI

Article

Health Monitoring and Fault Detection in Photovoltaic Systems in Central Greece Using Artificial Neural Networks

Elias Roumpakias and Tassos Stamatelos *

Department of Mechanical Engineering, University of Thessaly, 383 34 Volos, Greece
* Correspondence: stam@uth.gr; Tel.: +30-24210-74067

Featured Application: The health monitoring of a photovoltaic park is essential for a number of reasons, including early action to safeguard the profitability of investment and the timely support of claims regarding PV panels' performance degradation. This study was motivated by the previous, successful application of machine learning in the prediction of a photovoltaic plant's output based on monitoring data. An extension of these applications to the health monitoring and fault diagnosis of photovoltaic parks is proven successful, as demonstrated in this paper. The results are applicable to the systematic performance monitoring and fault detection of photovoltaic installations.

Abstract: The operation and maintenance of a photovoltaic system is a challenging task that requires scientific soundness, and has significant economic impact. Faults in photovoltaic systems are a common phenomenon that demands fast diagnosis and repair. The effective and accurate diagnosis and categorization of faults is based on information received from the photovoltaic plant monitoring and energy management system. This paper presents the application of machine learning techniques in the processing of monitoring datasets of grid connected systems in order to diagnose faults. In particular, monitoring data from four photovoltaic parks located in Central Greece are analyzed. The existing data are divided for training and validation procedures. Different scenarios are examined first, in order to observe and quantify the behavior of artificial neural networks in already known faults. In this process, the faults are divided in three main categories. The system's performance deviation against the prediction of the trained artificial neural network in each fault category is processed by health monitoring methodology in order to specify it quantitatively.

Keywords: photovoltaics; health monitoring; fault-detection; artificial neural networks

Citation: Roumpakias, E.; Stamatelos, T. Health Monitoring and Fault Detection in Photovoltaic Systems in Central Greece Using Artificial Neural Networks. *Appl. Sci.* **2022**, *12*, 12016. https://doi.org/10.3390/app122312016

Academic Editors: Isabel Santiago Chiquero, Isabel María Moreno García and Rafael López Luque

Received: 9 November 2022
Accepted: 22 November 2022
Published: 24 November 2022

1. Introduction

Worldwide growth in the installation of renewable energy systems has been remarkable during the last decade. The most popular and widespread renewable energy technologies in Greece are wind, photovoltaic (PV), biomass/biogas and hydropower. According to the Renewable Energy Sources Operator and Provider of Guarantees of Origin of Greece, the installed power is 4426.23 MWp for wind, 4198.59 MWp for photovoltaics, 112.31 MWp for biomass/biogas and 257.92 MWp for hydropower [1]. The design, operation and maintenance of renewable energy systems is a challenging task that requires measurement accuracy and scientific soundness in the processing of monitoring data. Monitoring data from these energy systems can give important information for a system's design and performance evaluation. Furthermore, data can be used in energy management either for fault detection or for power forecasting. The following are considered as the most critical problems related to energy optimization and maintenance in photovoltaic systems: Max Power Point Tracking, Output Power Forecasting, Parameter Estimation, Defect Detection [2]. A fault detection method for a PV energy system can provide an accurate estimation of production under normal operating conditions as well as hints for the detection of the system's faults [3]. Faulty operating conditions result in a reduction in energy production and compromise the reliability of the system, while creating financial losses for investors [4].

Many researchers have studied the fault detection of photovoltaic systems by combining measurements, experiment and computational methods. Every approach is characterized by the specific type of fault that detects the methodology addressing this task, and the specific application category. Faults concern both the AC side and DC side, as commonly observed in stand-alone and grid-connected PV systems [5]. Garoudja et al. categorized faults by: (i) short-circuit faults, that can affect cells, bypass diodes or modules, and the aging of PV modules; (ii) open-circuit faults that involve a break of wiring between PV modules or solar cells, and (iii) partial shading faults, which affect shaded modules, while the other part is normally exposed to solar irradiance, the passage of clouds, dirt on PV modules, snow, other light barriers and obstacles [6]. Other faults related to PV panels or panel covers involve: the fracture of the glass protective surface; bubbles and/or tears to the polymer cover of the backsheet; the corrosion of metallic frames; damage to the panel's insulation; failed soldering joints of the PV cells; hot spots; and the PID effect [7].

A large variety of techniques are applied to monitoring and measurement data management and processing. The multiple forms of machine learning (ML) are prominent in these techniques. ML may be broadly defined as the practice of using algorithms to parse data, learn from them, and then make a determination or prediction thereof [8]. Neural networks (NN) and statistical methods are the most frequent tool categories, applied in fault detection in the area of photovoltaic energy systems. Silvestre et al. proposed an algorithm procedure based on the comparison of simulated and measured yields. The main type of faults examined and traced are inverter disconnection, partial shadowing and the disconnection of a string. The method was applied in a 9 kWp PV test installation in Algeria [9]. Dhimish et al. proposed a procedure for automatic fault detection and diagnosis based on the statistical comparison of the means of measured and theoretical power using the *t*-test. The application and validation of this method was conducted in a 1.98 kWp system in United Kingdom [10]. Garoudja et al. propose a method for fault detection comparing measured values with simulated values by use of a one-diode model. The processing of the difference between the measurements and model predictions, used as fault indicators, was carried out through the application of an exponentially weighted moving average (EWMA) monitoring chart [6]. Another statistical approach is based on labeling faults at over 100 PV sites in the United States, by the use of machine learning (ML) algorithms and hidden Markov modeling (HMM), which allow the labeling of historical behaviors without a manual setting of threshold [11]. Chine et al. proposed a model for the detection of faulty modules in a string, faulty string, faulty inverter and false alarm, a group of faults which include partial shading, the ageing of PVs and inverter MPPT errors. The idea behind this method is the comparison of absolute error on the performance ratio (PR) with a threshold, that enables generating a diagnostic signal [12]. Research on the health monitoring of PV installations is profiting from the quite significant, parallel research efforts applied to the vibration-based health monitoring of civil structures, affected by environmental factors (traffic, ambient temperature, noise), which change their structural dynamic characteristics, covering up those coming from structural damage. For example, Huang et al. employed the support vector machine (SVM) and moth-flame optimization (MFO) [13], as well as an autoregressive (AR) time series model with two-step artificial neural networks (ANNs) [14] to identify damage under temperature variations. Suresh et al. compared the behavior of a multiple linear regression, ARMA model, CNN-simple, and CNN-LSTM and observed that the CNN-simple and the CNN-LSTM methods perform best for all 1-h, 1-day and 1-week predictions, with the CNN-LSTM providing better results on certain occasions [15].

Many researchers face the degradation problem with methods applied in specific experimental setups in off-grid operation. Fuster-Palop et al. proposed the use of simple machine learning tools to predict the global PR based on the following variables: global irradiance in-plane of array, and ambient temperature. Two regression models were applied: a multiple linear regression (MLR), and random forest (RF) algorithm, which is simpler than ANN [16]. Hichri et al. propose a machine learning method for fault diagnosis and classification, which is based on the principal component analysis (PCA) technique. The proposed approach is applied in a PV system comprising three 4 kWp PV arrays, each driven by individual MPPT trackers [17]. Ammiche et al. proposed a method based on a fuzzy logic filter (FLF), which relies on PCA and moving window principal component analysis (MWPCA). The method was applied in three inverters, with polycrystalline, monocrystalline and thin film PV panels connected, respectively, in Malaya University. The results demonstrate the method's effectiveness in detecting different types of faults with high accuracy [18]. Cui et al. proposed a PV-fault identification method based on improved deep residual shrinkage networks (DRSN). The method was able to identify short-circuit faults, partial-shading, abnormal aging and hybrid faults in a 6.48 kWp experimental PV field [19]. Voutsinas et al. proposed a multi-output ANN for fault detection on the DC side of a photovoltaic system. A comparison of I_{mpp} and V_{mpp} values, obtained from the models based on data from the manufacturer's data sheets, proved the effectiveness of the proposed method [20]. Guejia Burbano et al. propose an ANN for faults and degradation phenomena occurring in PV panels. The method has two stages: one for predicting the single diode model parameters under normal operation, and one for the degraded condition. Comparison between the two stages is used for the identification of the degradation type. The method was tested using experimental data of I-V curves from the NREL database [21]. Hopwood et al. propose an approach that utilizes physics-based simulations of string-level IV curves. Comparison between a baseline curve (no fault) and cases with partial soiling and cell crack system modes are presented [22]. Wang et al. proposed a hybrid algorithm by combining the symmetrized dot pattern (SDP) with a convolutional neural network (CNN) for common faults such as poor welding, breakage and bypass diode failure. Comparison with a fault-free module was conducted and this study successfully combined SDP with CNN to develop a PV module fault, with recognition accuracy reported to 99.88%.

On the other hand, methods to be applied in a grid-connected operation were also presented. Hichri et al. developed a genetic-algorithm (GA)-based ANN. The proposed method is applied in GCPV systems under normal and faulty conditions [23]. Aljafari et al. created a detection technique based on the comparison of calculated and measured DC power, with a predefined threshold value. The method uses a simulation tool for calculated values and generates a diagnostic signal to show normal or abnormal operation in a 2 kWp GTPV plant [24]. Hussain et al. propose a simple technique for the detection and classification of faults occurring in PV systems based on a fuzzy logic controller. The method introduced a 'fault index', which measures the degree of deviation from the normal operating conditions and is applied in a 5 kWp grid-connected PV system [25]. Another aspect of fault detection aims in special types of faults as faulty inverters' operation and problems with arc discharge at the DC side. Wang et al. proposed a fault detection method for DC series arcs based on the combination of adaptive local mean decomposition (ALMD), multiscale fuzzy entropy (MFE), and support vector machine (SVM) algorithms for PV systems [26]. Omana et al. propose a model for the detection of inverters' faults, especially those observed at the inverter's power MOSFETs. The method is based on periodically monitoring the variation in the harmonics of the inverter's currents [27]. Improved fault detection algorithms are also comparatively tested by Hussain et al. [28] in small pilot PV installations by the use of non-iterative FF ANN and radial basis function (RBF) ANN. Further development in the topology and training algorithms include non-iterative neural-like structures based on the successive geometric transformations model (SGTM), which has been successfully applied to big data in regression and classification tasks in related sectors [29].

Finally, IR thermography is a method that gives motivation to a fair number of researchers. Álvarez-Tey et al. proposed an IR thermography inspection strategy for PV plants based on a two stage aerial inspection and carried out on the ground. The method was applied to a 100 kW PV plant. The types of faults addressed were broken glass in a PV module, partial shading, problems involving PV module technology and open-circuit PV modules, along with other incidents [30]. Kim et al. proposed an algorithm in order to analyze the infrared images of solar panels. The proposed method uses a convolutional neural network with SVM (CNN-SVM) to classify enhanced images in order to conduct non-physical visual recognition and fault detection analysis [31].

The current work focuses to the application of ANN in the fault detection of grid-connected PV plants. The main contribution is the analysis and evaluation of already known fault types on grid- connected systems with the aid of ANN, aiming at formulating a procedure to enable fault diagnosis through the quantification of statistical metrics characteristic to each type of fault. To this end, the evaluation of the same type of ANN with different inputs is carried out. The novelty of the proposed methodology is based on the correlation of already known faults in grid-connected PV systems, with the statistical deviation of their performance metrics when they are observed with the aid of an ANN.

The organization of the remaining part of this paper is as follows: Section 2 presents the testing setup and the fault detection methodology. Section 3 presents and discusses the results of its application to normal operation, as well as to its operation with various known faults. A discussion follows in Section 4, which defines the error tolerances to be associated with each fault category. Finally, Section 5 summarizes the main findings with the methodology developed, its limitations and prospects for future research.

2. Materials and Methods

The experimental and monitoring set up and methods implemented for fault detection using data from three grid-connected photovoltaic systems in Greece are described in this section.

2.1. Experimental Setup

The available data for testing our fault detection approach are provided by three grid-connected photovoltaic system of 99.84 KWp on central Greece. Each system consists of 8 inverters and 416 PV panels on the park, mounted in a fixed south facing position with 25 degrees' tilt angle. The technical characteristics of the equipment are presented in Appendix A. All systems have the same layout and equipment, something that is important for the comparative analysis that follows. The available measurements are irradiance, back panel temperature, ambient temperature, DC voltage and AC power from inverter inlet. The dataset covers a period of 4 years (1 January 2013–31 December 2016) of operation. The monitored performance parameters of the PV installation are recorded in a data logger at 15 min intervals. The main technical characteristics of the PV system are shown in Appendix A. An important detail in the system's design that should be mentioned here, is the lack of a cleaning system for the panels' surfaces.

2.2. Methodology

The basic building block for the proposed methodology is a performance analysis procedure already described in [32]. The first step of the methodology involves a quality control process of the available data. The main criteria for cleaning the data are specified in terms of limit values of irradiance, airmass and power output of each inverter. Zero values of inverter power output are rejected, along with irradiance values < 50 W/m^2. Airmass is an important parameter affecting performance, as detailed in [33], where it is explained why data with $AM > 10$ are rejected. The second step of the methodology is the training procedure of an ANN, using monitoring data from the year 2013. A feed forward artificial network with two input parameters and a hidden layer with 20 neurons is applied. This is a simple and effective form of ANN that produces fast and reliable results with acceptably high accuracy for the purposes of this fault detection procedure, without requiring significant computational resources. The structure of the FF ANN is shown in Figure 1.

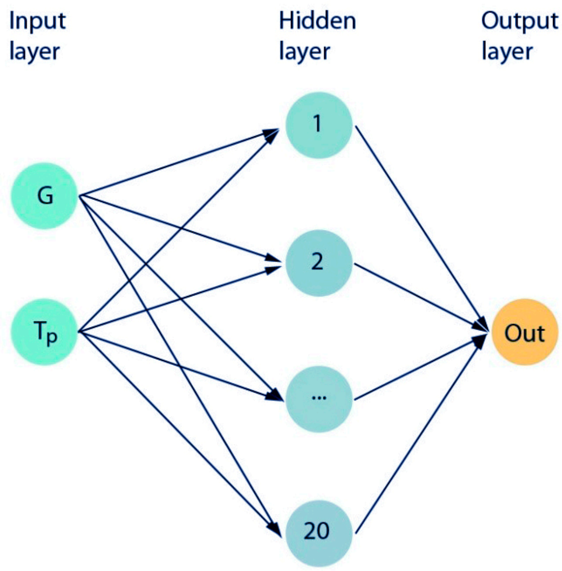

Figure 1. Structure of the feed-forward artificial neural network.

The model's input parameter models are: (i) in-plane irradiance; and (ii) panel back-sheet temperature or ambient temperature, depending on the availability of the respective sensor. The model's output is AC power, which is also set as the target in the training procedure. The next step is to conduct simulation with the trained ANN, formulated in specially designed experimental scenarios. The behavior of these simulations is observed in the period (2014–2015) against the available data.

The most important parameters of the FF ANN design are presented in Table 1, along with the hyper-parameters related to the training procedure, which uses a network training function that updates weight and bias states (expressed in vector form $\mathbf{x}_k$) according to the well-known Levenberg-Marquardt back propagation optimization algorithm [34]:

$$\mathbf{x}_{k+1} = \mathbf{x}_k - \left[\mathbf{J}^T(\mathbf{x}_k)\mathbf{J}(\mathbf{x}_k) + \mu_k \mathbf{I}\right]^{-1} \mathbf{J}^T(\mathbf{x}_k)\mathbf{v}(\mathbf{x}_k) \tag{1}$$

where $\mathbf{J}$ the Jacobian matrix, μ_k the current value of mu at step k, and $\mathbf{v}(\mathbf{x}_k)$ is the vector of the components of the performance index (sum of squares). This algorithm has the very useful feature that as μ_k is increased, it approaches the steepest descent algorithm with small learning rate [34]:

$$\mathbf{x}_{k+1} \cong \mathbf{x}_k - \frac{1}{\mu_k}\mathbf{J}^T(\mathbf{x}_k)\mathbf{v}(\mathbf{x}_k) = \mathbf{x}_k - \frac{1}{2\mu_k}\nabla F(\mathbf{x}) \tag{2}$$

while as μ_k is decreased to zero the algorithm becomes Gauss-Newton.

The algorithm begins with $\mu_k = 0.001$ (Table 1). If a step does not yield a smaller value for the performance index, the step is repeated with μ_k multiplied by a factor of 10 (Table 1). If a step reduces the performance index, then μ_k is divided by 10 for the next step. Thus, we would move closer to Gauss-Newton, to provide faster convergence. The algorithm provides a nice compromise between the speed of Newton's method and the guaranteed convergence of steepest descent.

Three instances of the same FF ANN are trained independently based on three sets of data (n_1, n_2, n_3), which correspond to the output of three different inverters from PV plants in Central Greece. All three PV plants examined share the same layout and equipment types, which are presented in Appendix A. Table 2 summarizes the characteristics of the three systems employed for training the three independent FF ANN n1, n2 and n3.

Table 1. Design parameters of the specific type of FF ANN applied, along with the hyper-parameter values related to the training procedure.

ANN Type	FF
ANN Dimensions	
Inputs	1
Layers	2
Outputs	1
Input Delays	0
Layer Delays	0
Weight Elements	81
ANN connections:	
Bias Connections:	[1; 1]
Input Connections:	[1; 0]
Layers Connections:	[0 0; 1 0]
Output Connections:	[0 1]
ANN Training hyper-parameters	
Maximum Epochs	1000
Maximum Training Time	Inf
Performance Goal	0
Minimum Gradient	1.00×10^{-7}
Maximum Validation Checks	6
μ_k	0.001
μ_k decrease ratio	0.1
μ_k increase ratio	10
Maximum μ_k	1.00×10^{10}

Table 2. Characteristics of the three FF ANNs and their respective PV systems.

Network	PV Plant	Inverter	Input Parameters	Training Period
n1	PVS1	INV4	Irradiance Back Panel Surface Temperature	2013
n2	PVS2	INV3	Irradiance Back Panel Surface Temperature	2013
n3	PVS3	INV6	Irradiance Ambient Temperature	2013

The values of statistical metrics are used as indicators of faults. Statistical metrics are calculated either on a daily or on an annual basis. However, the daily values are the main indicators of faults. Statistical metrics that are used for results comparison are the root mean square error (RMSE), the normalized root mean square error (nRMSE), the mean absolute error (MAE), the mean absolute percentage error (MAPE) [35], the mean bias error (MBE) [36] and the Pearson correlation coefficient [37]:

$$\mathrm{RMSE} = \frac{1}{\mathrm{N}}\sqrt{\sum_{\mathrm{i}=1}^{\mathrm{N}}(\mathrm{P}f_{\mathrm{i}} - \mathrm{P}m_{\mathrm{i}})^2} \tag{3}$$

$$\mathrm{nRMSE} = \frac{\sqrt{\sum_{\mathrm{i}=1}^{\mathrm{N}}(\mathrm{P}f_{\mathrm{i}} - \mathrm{P}m_{\mathrm{i}})^2}}{\sqrt{\sum_{\mathrm{i}=1}^{\mathrm{N}}(\mathrm{P}m_{\mathrm{i}})^2}} \tag{4}$$

$$\mathrm{MAE} = \frac{\sum_{\mathrm{i}=1}^{\mathrm{N}}|\mathrm{P}f_{\mathrm{i}} - \mathrm{P}m_{\mathrm{i}}|}{\mathrm{N}} \tag{5}$$

$$\mathrm{MAPE} = \frac{100\%}{\mathrm{N}}\sum_{\mathrm{i}=1}^{\mathrm{N}}\frac{|\mathrm{P}f_{\mathrm{i}} - \mathrm{P}m_{\mathrm{i}}|}{\mathrm{P}m_{\mathrm{i}}} \tag{6}$$

$$\mathrm{MBE} = \frac{\sum_{i=1}^{N}(Pf_i - Pm_i)}{N} \quad (7)$$

$$\mathrm{PBIAS} = 100\% \frac{\sum_{i=1}^{N}(Pf_i - Pm_i)}{\sum_{i=1}^{N}(Pm_i)} \quad (8)$$

$$\mathrm{COR} = \frac{\mathrm{COV}(Pm_i, Pf_i)}{\sqrt{V(Pm_i)}\sqrt{V(Pf_i)}} 100\% \quad (9)$$

The next step is the correlation of statistical metrics with already known faults in each PV system. These may concern a fault in one of the four strings connected to each inverter (see details in Appendix A), faults in a single PV panel, shading during specific days of year close to the winter solstice. It is important to understand first the networks performance in normal operation, by observing the behavior of statistical metrics in order to establish a performance baseline. Furthermore, the application of ANN to different inverters and different PV systems allows the clear establishment of specific thresholds in the statistical performance metrics that points to the detection of specific types of faults. Different scenarios are employed in this work in order to demonstrate the use of the fault detection methodology. Another important metric that is computed and employed in the methodology is the performance ratio, as described in Appendix B.

3. Results

In this section, different scenarios of ANN application are presented for normal and faulty operation. It is important to discuss and analyze the results to support the fault detection methodology. An important parameter here is the number of measurement sets employed, in order to increase confidence in the fault detection findings in the results.

3.1. Normal Operation

First, the performance data of the PVS1 system are applied to the ANN n1. The network n1 is trained by data of inverter 4 of PVS1. Simulated values are compared with measured values from inverter 4 and the results are presented in Figure 1. The PBIAS fluctuated between −3.7 to 1.2 and nRMSE between 2.23 to 5.05 according to Table 3. The size of the samples involved in the daily calculations varied from 47 to 53.

Table 3. Statistical metrics of the inverter 4 of PVS1 for the period 5 June 2014 to 17 June 2014 (normal operation).

Date	N	RMSE	MBE	MAPE	MAE	nRMSE
2014-06-04	47	22.69	103.74	3.07	109.36	3.91
2014-06-05	51	23.49	102.59	1.65	118.47	2.33
2014-06-06	50	40.39	190.42	3.30	213.82	4.36
2014-06-07	51	26.35	130.98	2.20	154.16	2.81
2014-06-08	49	33.76	171.73	3.70	172.06	4.16
2014-06-09	49	21.63	106.82	2.68	119.55	3.25
2014-06-10	49	24.15	117.27	1.84	143.88	2.36
2014-06-11	50	36.67	74.18	1.20	129.42	3.74
2014-06-12	48	47.54	150.79	2.61	194.21	5.05
2014-06-13	49	22.07	88.65	1.55	103.63	2.40
2014-06-14	49	27.99	152.86	3.34	152.86	3.58
2014-06-15	48	26.05	149.96	3.60	150.29	3.39
2014-06-16	50	21.29	74.08	1.22	119.36	2.23
2014-06-17	53	17.85	115.58	3.65	115.58	3.37

Figure 2 shows the fitting quality of the simulated and actual values in normal operation. The daily mean absolute error varies in the range from 103.63 to 213.82 W. The peak DC power in each inverter is 12,480 W and the maximum AC values for the respective period presented in Figure 1 did not exceed 11,000 W. The values of the statistical metrics that express the fitting accuracy are detailed in Table 3. The reported values of nRMSE, MAPE and the number of samples define a threshold for normal operation. Deviation from these values may indicate a possible fault. Especially, the values of MBE are positive, indicating a systematic over-prediction of output. These facts operate as indicators for faults either in PV system or in measurement equipment.

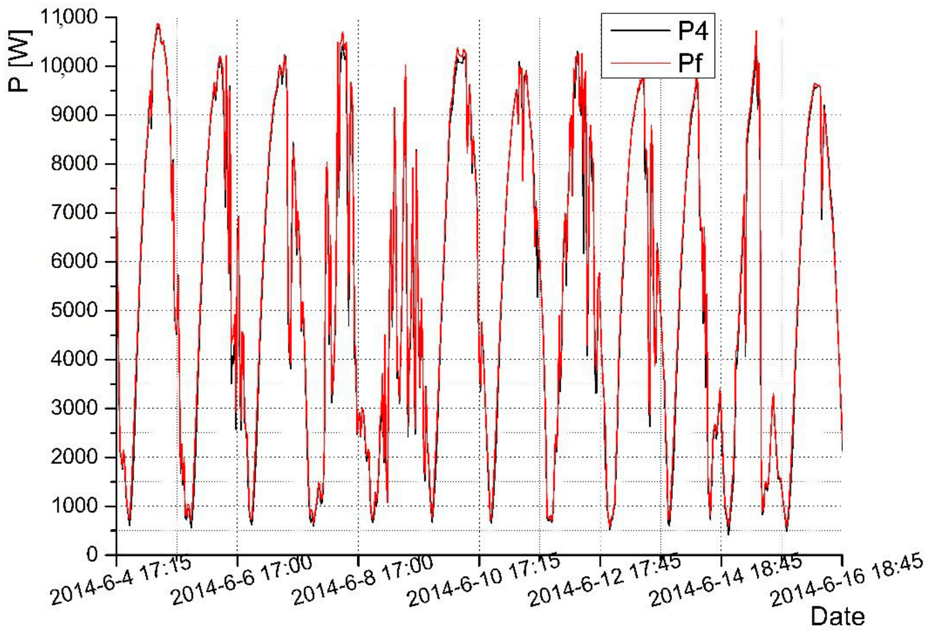

Figure 2. Comparison between the measured AC power values at inv4 and the simulated values during several days in mid-June.

According to the obtained statistical metrics of Table 3, the FF ANN fits the data with acceptable accuracy, since both MAPE and nRMSE are well below 5%. Adopting deep neural networks as CNN could further improve accuracy. However, what is important here is to set the basis for a fault detection methodology, where the obtained accuracy suffices and the fast convergence with low computational expenditure is very desirable. It is important to investigate the behavior of the other inverters of the same system when compared to simulated values for n1 network, which is trained from inverter 4. In Figure 3, a comparison in power output of eight inverters is compared to the respective simulated values.

A comparison of the simulated values (Pf) with those measured at all inverters of PVS1 (Figure 3) indicates a very good agreement. The MAPE of the other inverters fluctuated between 0.06–3.56, while nRMSE 1.57 to 3.29%. The precise values of the statistical deviations shown in Table 4 indicate that MAPE and nRMSE of inverter 4 are at the same levels. This fact proves that an ANN simulation trained for one inverter of the n1 network in normal operation matches with high accuracy the behavior of all inverters. As shown in the technical data of the Appendix A, each inverter has the same number of strings, same number of panels and same type of PV panels.

Table 4. Statistical metrics: MAPE and nRMSE for all inverters of PVS1 for the dates presented in Figure 3. Inverter 4 is not included since it was employed as a training target.

		Inv1	**Inv2**	**Inv3**	**Inv5**	**Inv6**	**Inv7**	**Inv8**
	N	MAPE	MAPE	MAPE	MAPE	MAPE	MAPE	MAPE
2014 06 13	49	2.25	2.08	1.57	1.83	1.22	1.29	0.06
2014 06 14	49	3.49	3.56	2.92	3.15	2.48	2.89	1.51
	N	nRMSE	nRMSE	nRMSE	nRMSE	nRMSE	nRMSE	nRMSE
2014 06 13	49	2.86	2.72	2.45	2.33	1.96	2.00	1.57
2014 06 14	49	3.18	3.29	3.03	3.31	2.83	3.09	2.08

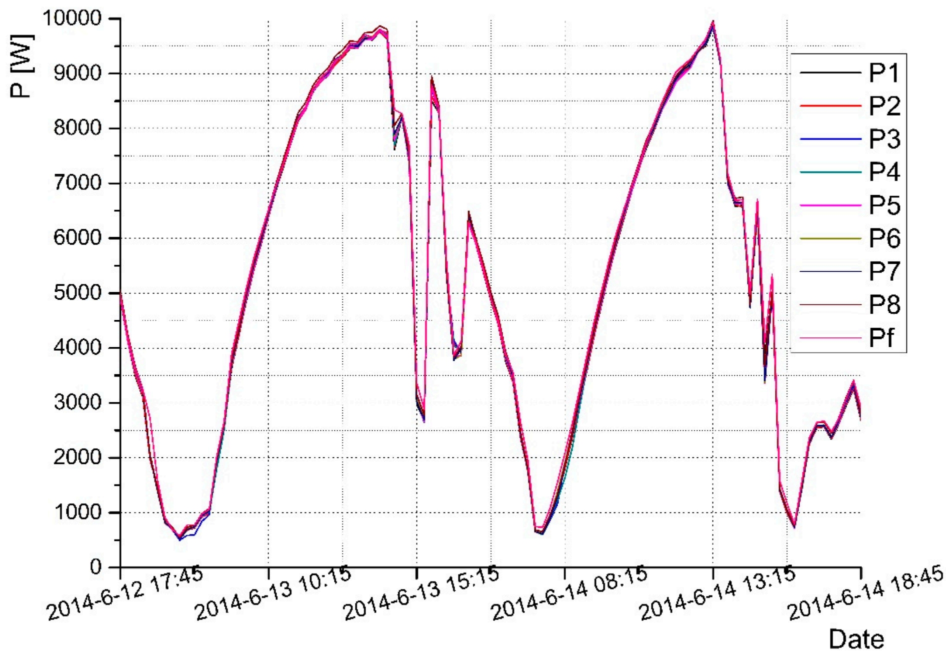

Figure 3. Comparison between the measured power at all inverters of PVSE and simulated values during two consecutive summer days.

The above findings, for normal operation, are summarized as follows: the nRMSE values fluctuated in the range 1–5%, where 5% can be considered as a threshold not to be surpassed during normal operation. The respective MAPE are in the range from 0.06 to 3.56. The values of the specific statistical metrics in normal operation may be employed as a reference for the analysis of faults that are presented below.

3.2. String Fault Behavior

In this section, the situation resulting from a fault in a DC fuse is examined. Each inverter has four strings which are connected to the inverter with fuses. From 4 April 2015 to 9 April 2015, the values of nRMSE are observed to exceed 30% during the period when the fault occurred, as seen in Table 5. The maximum value was observed on 9 April, 2015, when the inverter operation was shut down in order to replace the fuse. The respective values of the MAPE, MAE and MBE are all at significantly higher levels than in normal operation. This effect is also observed in Figure 4, where the simulated and measured values are compared. Furthermore, the values of PR, which is an important performance metric, are observed to be significantly lower in Table 5 for the specific days.

Table 5. Statistical metrics of inverter 8 of the same PVS1 from 1 April 2015 to 11 April 2015 for abnormal operation.

	N	RMSE	MBE	MAPE	MAE	nRMSE
01/04/15	45	58.61	215.09	3.08	251.04	5.09
02/04/15	45	62.81	304.49	4.09	314.49	5.09
03/04/15	42	59.12	335.71	4.50	335.76	4.62
04/04/15	44	174.18	739.61	11.50	740.57	15.75
05/04/15	44	98.18	539.20	36.80	539.20	37.00
06/04/15	44	277.98	1485.23	38.45	1485.23	38.53
07/04/15	44	281.74	1546.18	38.87	1546.18	39.19
08/04/15	41	267.69	1420.66	37.78	1420.66	38.52
09/04/15	46	324.78	1144.33	21.54	1156.98	36.13
10/04/15	46	43.04	185.39	2.45	242.91	3.51
11/04/15	46	26.80	102.07	1.37	159.63	2.24

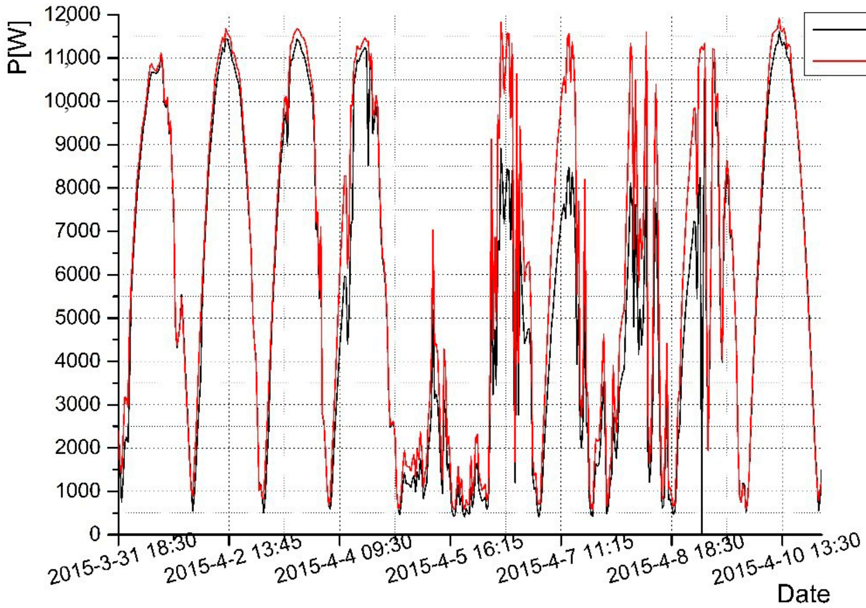

Figure 4. Actual output of inverter 8 (PVS1), compared with the ANN simulated output from n1, for the period 1 April 2015 to 11 April 2015 (abnormal operation due to faulty DC fuse observed from 5.4 to 9.4).

A closer observation of the simulated and actual operation in Figure 4 allows to visualize how the onset of faulty operation occurs, after an initial period of normal operation. The deviation between simulated and real power is clear even for a cloudy day, 5 April 2014. Comparing statistical metrics for the period of normal operation with those for the faulty operation period, the remarkable deviation between simulated and actual performance observed for the days where this type of error occurs corresponds to error levels exceeding 30%, both with regard to the nRMSE and MAPE. This is also depicted in the daily energy production and PR of the deviation between simulated and actual values, presented in Table 6.

Table 6. Energy production and PR for the period 1 April 2015–11 April 20215.

	kWh	PR
1/4/15	78.48	0.88
2/4/15	83.71	0.89
3/4/15	78.35	0.91
4/4/15	70.74	0.84
5/4/15	16.11	0.71
6/4/15	42.48	0.67
7/4/15	43.78	0.69
8/4/15	38.52	0.72
9/4/15	61.08	0.78
10/4/15	86.93	0.92
11/4/15	85.46	0.89

This type of fault is inspected in PVS3 with the aid of ANN network n3 that is trained with ambient temperature and irradiance as inputs. Values of n RMSE > 30% may be safely correlated with the same error in one string of the inverter as it is observed from ANN n1, which differentiates in the type of temperature received as input. This is depicted in Table 7 and Figure 4, and is also validated from PR decrease (Table 8).

Table 7. Statistical metrics of the deviation between two inverters of the same PVS during June of 2014 for normal operation.

	N	RMSE	MBE	MAPE	MAE	nRMSE
05/08/14	47	16.93	75.32	1.25	90.94	1.68
06/08/14	33	33.29	74.45	1.14	132.52	2.62
07/08/14	45	67.79	183.60	2.81	238.89	6.33
08/08/14	47	28.66	94.47	1.50	117.19	2.83
09/08/14	47	126.29	527.04	9.11	545.98	13.39
10/08/14	47	86.39	319.13	5.26	355.21	8.78
11/08/14	48	52.94	201.50	3.23	214.42	5.31
12/08/14	47	121.90	437.72	7.01	505.55	12.17
13/08/14	47	282.27	1785.43	34.55	1785.43	34.76
14/08/14	47	234.86	1437.11	33.06	1437.11	32.18
15/08/14	47	311.10	1776.26	33.24	1776.26	36.30
16/08/14	47	20.83	76.51	1.11	127.83	1.92
17/08/14	47	20.92	87.47	1.40	124.32	2.07
18/08/14	47	23.92	132.15	2.28	142.06	2.54

Table 8. Statistical metrics of the deviation between two inverters of the same PVS during June of 2014 for normal operation.

Date	kWh	PR
8/8/2014	70.58	0.85
9/8/2014	76.24	0.86
10/8/2014	73.98	0.83
11/8/2014	73.92	0.85
12/8/2014	67.50	0.79
13/8/2014	70.73	0.82
14/8/2014	73.37	0.83
15/8/2014	70.86	0.80
16/8/2014	58.26	0.63
17/8/2014	47.94	0.65
18/8/2014	59.48	0.65

Figure 5 shows a comparison between the simulated and actual behavior of AC power output during a normal operation period that is followed by faulty operation. A statistically significant deviation between simulated and actual power output is observed from 13 August 2014 to 15 August 2014. Significant deviations are also observed on 16 April 2014, when an inverter shut-down became necessary in order to repair the fault. Comparing the statistical metrics of normal operation with faulty operation, we observe the same remarkable deviation of over 30% in nRMSE and MAPE, as in case of PVS1. This is also depicted in the daily energy production and PR values of Table 7.

The above observations point to the conclusion that a faulty operation in a string is confirmed when n1 and n3 demonstrate the same type of behavior, despite the fact that these networks have different temperature inputs. The values of nRMSE fluctuated over 30% when the error occurred all day round. The same behavior was observed with the respective values of MAPE.

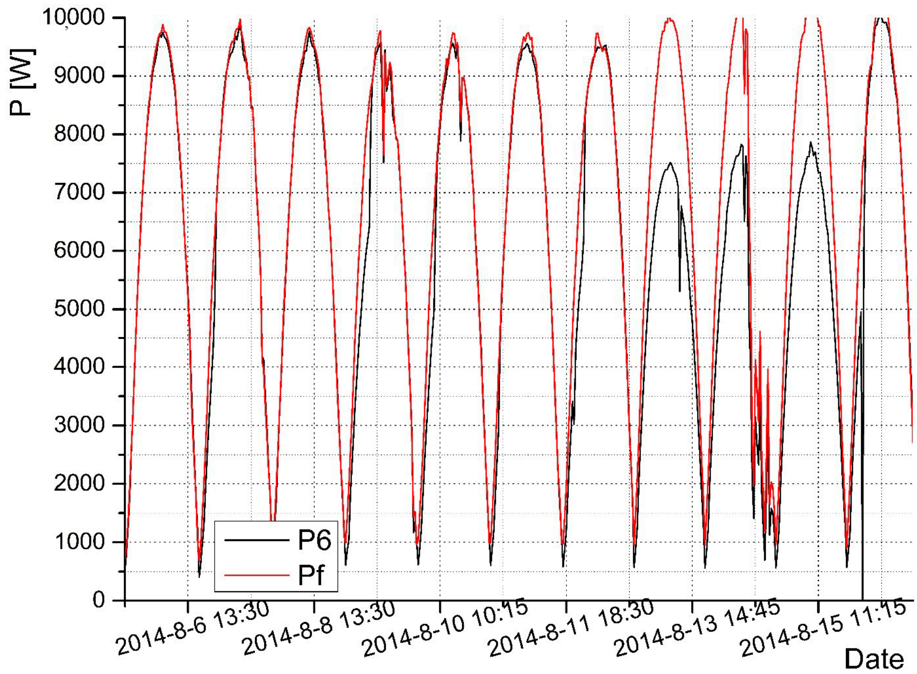

Figure 5. Fault in a string during June 2014.

3.3. PV Panel Fault Diagnosis

In this section, an inspection of the effects of a well-known fault in a PV panel, which is a fracture of its surface, is carried out. It is not accurately known at what time the fault emerged, however, it is known that the fault panel was replaced on 4 November 2015. According to the analysis, it may be observed that the onset of the fault took place at the end of March. This was also confirmed during an IR thermography testing. In this section, the n2 network is trained by data of inverter 3 of PVS2, where the fault panel was connected. This problem has smaller errors than the problem string panel that fluctuated between 15–20%. The statistical deviation between real and calculated value is presented in Figure 6 by means of the nRMSE, and Figures 7 and 8 by detailed comparison.

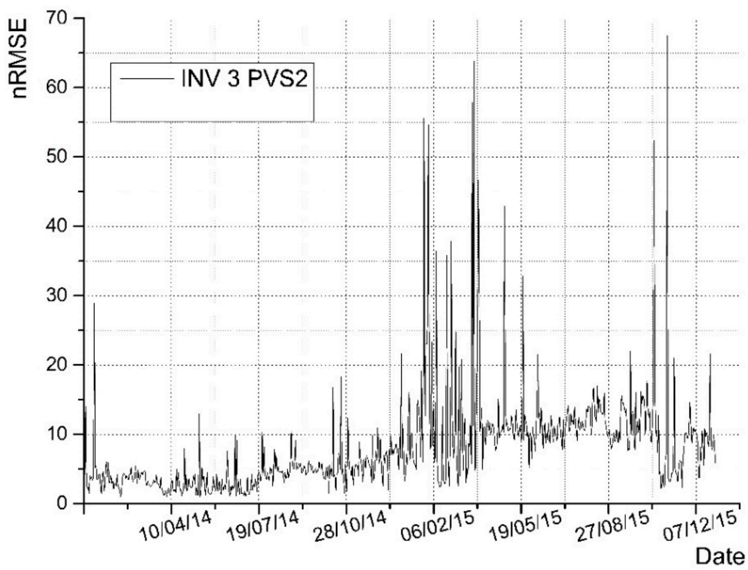

Figure 6. Evolution of NRMSE error during years 2014–2015.

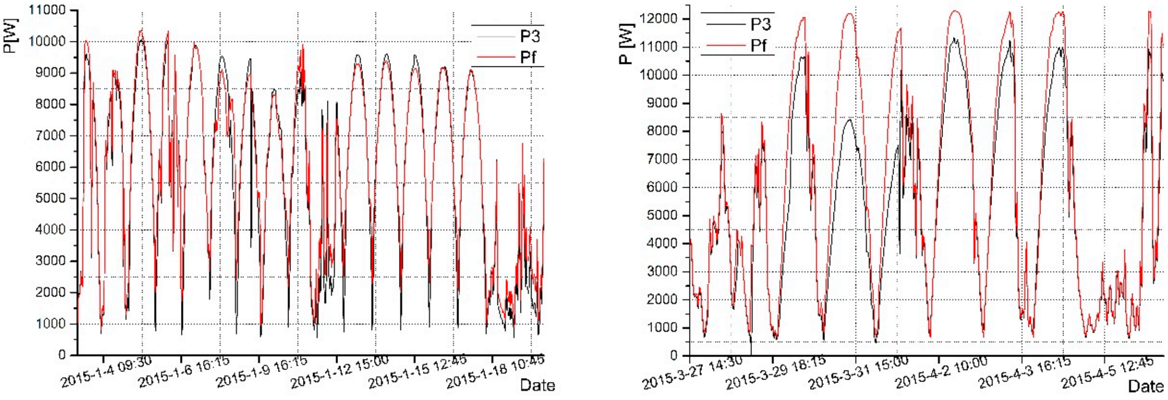

(**a**) (**b**)

Figure 7. Comparison between the actual power output and simulated values for different seasons of the year 2015: (**a**) in January and (**b**) in March–April.

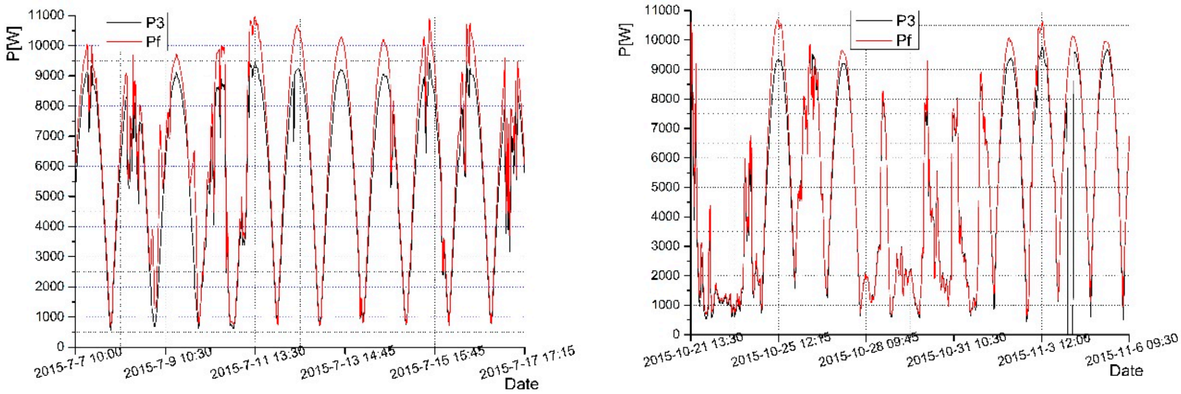

(**a**) (**b**)

Figure 8. Comparison between the actual power output and simulated values for different seasons of the year 2015: (**a**) in July and (**b**) in October–November.

The error trend is observed to be increasing by the end of March, where error values generally exceed 10%. If a threshold of 5% in nRMSE error is considered, it is clear that starting from February of 2015 error values steadily exceed this level. On the other hand, error values do not exceed 30%, which would be indicative of a fault in a string. Figures 7 and 8 confirm this observation, since the simulated values are constantly higher in March, July and October, rather than January (that was probably before the onset of the fault).

The fault causes significant deviation, especially in midday, when the levels of irradiance are higher and, respectively, temperature values. The temperature behavior of a faulty PV panel may affect the DC voltage of the string in which it is connected. Significant deviation in DC voltage may affect MPP tracker operation and consequently power output in these conditions. This type of fault also has significant impact on the statistical metrics, which allows it to be reliably quantified. Values of 10–20% in nRMSE are observed, which may be considered as an indicator of similar faults in a PV panel belonging to the specific string.

3.4. Shading Fault Diagnosis

In this section, the shading effect between arrays is analyzed, which is particularly observable during some days with small solar altitude, especially those in the second half of December. Actual and simulated AC power output is compared from 21 December 2015 to 27 December 2015 and are presented in Figure 9. The nRMSE values are in the range from 6.0 to 9.7%, as presented in Table 9. These error levels are the smallest compared to the faulty panel and faulty string errors.

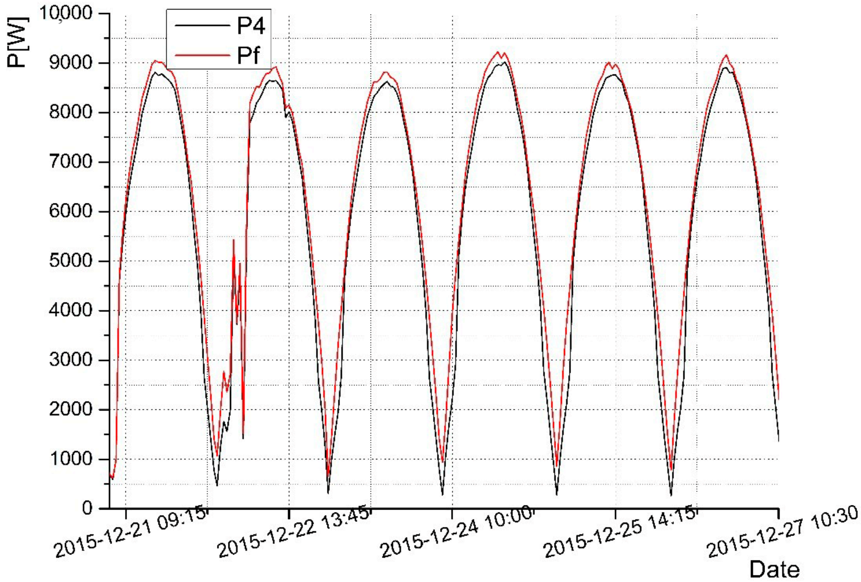

Figure 9. Comparison between real power output and simulated values for December 2015.

Table 9. Statistical metrics of inv4 PVS1 during December 2014, following the winter solstice.

	N	RMSE	MBE	MAPE	MAE	nRMSE
21/12/15	32	80.28	368.84	5.98	370.46	6.8
22/12/15	32	84.85	384.53	6.52	384.53	7.4
23/12/15	33	91.23	402.75	6.74	402.75	8.1
24/12/15	33	107.74	457.18	7.44	457.18	9.1
25/12/15	33	113.20	466.03	7.88	466.03	9.9
26/12/15	33	108.02	454.63	7.86	454.63	9.6
27/12/15	32	107.14	450.87	8.07	450.87	9.7
28/12/15	32	96.78	415.75	7.41	415.75	8.8

Figure 9 compares the simulated and actual behavior of the AC inverter output for the last days of December, 2015. However, the statistical deviation observed does not clearly point to a specific fault, as was the case with the previously reported cases, where the deviation source was recognizable. The fluctuation of nRMSE is in the range from 6.8 to 9.9%, which is close to the threshold of 5%. The PBIAS is observed to range from 5.98 to 8.07%, respectively. This fault cannot be easily correlated to a specific fault; however, it is important to estimate its deviation and compare it against several possible shading problems from obstacles, occasionally observed during the annual PV park' s operation, especially in rooftop PV installations in buildings.

4. Discussion

In the previous section, the different types of faults were presented and the behavior of nRMSE values seen as indicators of already known faults was discussed. It is also important to evaluate the behavior of ANN when they are fed with inputs from other PV systems. To this end, we present the behavior of all three networks in 2014, when they are fed with data from PVS1 (Figure 10).

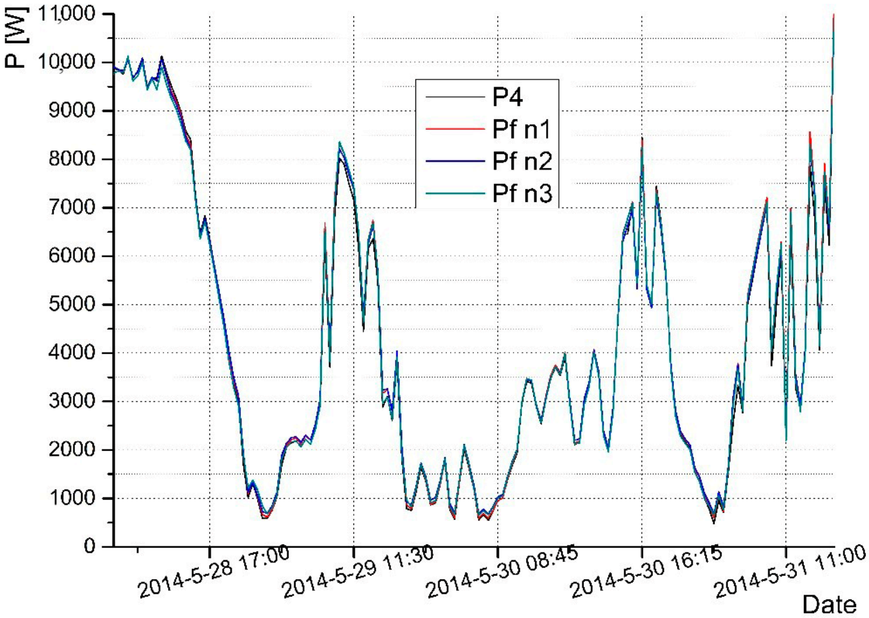

Figure 10. Comparative behavior of three ANNs fed with data from PVS1.

The specific behavior of all three networks during 2014 is statistically evaluated by the variation of nRMSE in this period.

Figure 11 shows a similar behavior for all three models. However, certain periods are observed with an increasing trend, except those correlated with the existence of a fault. This trend is significant at the end of March, when the nRMSE is seen to significantly increase. During this period, the n3 network, which has a different type of temperature sensor's input, demonstrates smaller deviations. This behavior is also observable in Figure 12. All three networks underestimate the simulated power, as seen in Figure 12. This may indicate an error in measurement equipment in network n3.

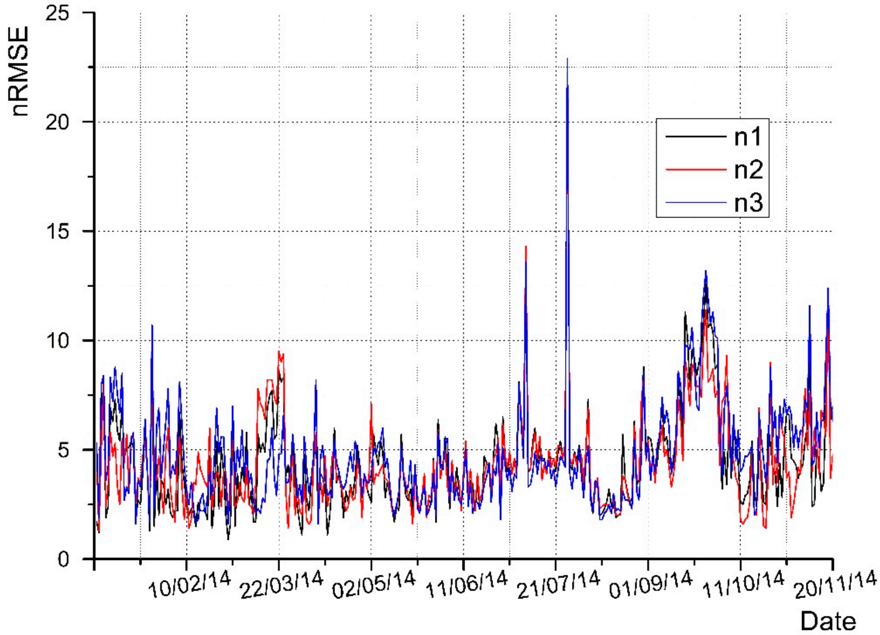

Figure 11. Comparison of n RMSE values for three ANNs during 2014.

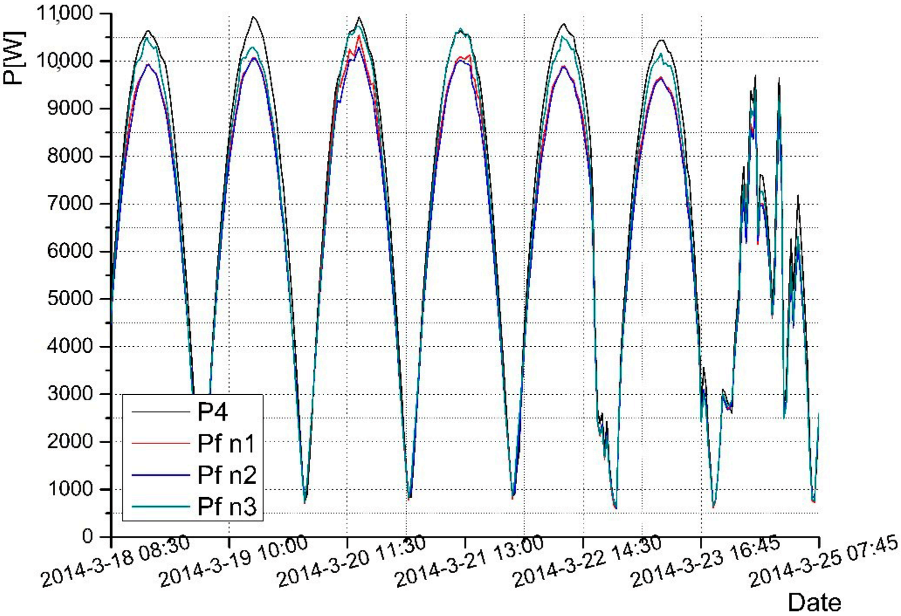

Figure 12. A period at the end of March in which all three networks are seen to underestimate the AC power output.

Figure 13 shows the trend of percent bias error during 2014. The general trend shows that simulated values are higher than the actual values; however, there are periods at the end of March where the result is the opposite. This fact may be related to a systematic error of measurement equipment in this period. The fact that n3 has a more consistent behavior in this aspect may indicate that this is an error in the backsheet temperature sensor.

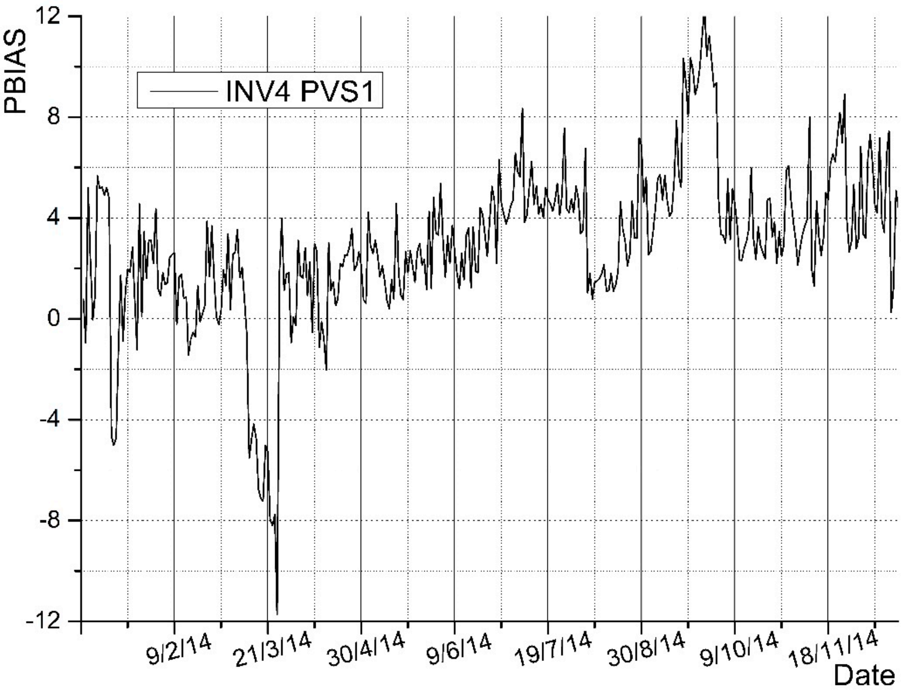

Figure 13. Evolution of percent bias of prediction during the whole year, 2014.

An observation of the nRMSE and PBIAS error values points to the fact that these metrics could act as indicators for possible faults. The behavior of these values (daily) in normal operation sets a clearly observable threshold. A fault in a PV string has the larger statistical deviation from ANN simulation to actual behavior, over 30%, fault panel has a deviation of 10–20% and faults of near shading 6–10%, compared to 5% during normal operation. These deviations are dependent on the specific system type, layout, location and the type of measurement equipment. However, the proposed procedure is valid—mutatis mutandis—in all these cases.

5. Conclusions

This paper employs datasets from performance monitoring of grid-connected PV systems in order to diagnose faults. Available data from three PV systems in central Greece, which have the same type of equipment, provide the possibility to analyze already known faults with the aid of a feed-forward artificial network, aiming to quantify the effect of these faults in the statistical metrics. The Levenberg-Marquadt optimization algorithm is proven capable to perform the ANN training to predict the AC inverter's output at normal operation, with fast convergence to nRMSE well below 5%. The quantitative identification of each type of fault is employed to support a diagnostic procedure, which is under development. Three types of faults are examined: a fault in a string of an inverter, a fault in a PV panel, and near shading faults. The nRMSE values pertaining to a fault in a string were over 30%, those induced by a fault in a PV panel were 15–20%, near shading fault were 6–9%. Thus, the loss of accuracy is significant and quite noticeable at the onset of each one of the fault types examined. A second important conclusion is that percent bias may be employed as a good indicator of a possible fault in the monitoring/measurement equipment. A third important finding is that the application of an ANN trained by a specific inverter's output, may be reliably employed in checking the performance of another inverter with the same installed power, technology and located at nearby locations. Finally, a parallel application of two networks with different inputs may diagnose faults in measurement equipment, a fact that may significantly improve the fault diagnosis procedure. The limitations of the proposed approach exist in the diagnosis of faults that have smaller and more gradual impact in PV energy production. These include soiling or dust accumulation and the gradual degradation of the PV panels. Future work will include an integration of these factors in the health monitoring methodology by the exploitation of datasets covering 10 or more years of the PV system's operation.

Author Contributions: Conceptualization, E.R. and T.S.; methodology, E.R. and T.S.; software, E.R.; validation, E.R.; formal analysis, E.R.; investigation, E.R. and T.S.; resources, T.S.; data curation, E.R.; writing—original draft preparation, E.R.; writing—review and editing, T.S. All authors have read and agreed to the published version of the manuscript.

Funding: This research received no external funding.

Conflicts of Interest: The authors declare no conflict of interest.

Appendix A

Table A1. Technical data of the PV modules.

Yingli 60 Cell YGE SERIES			
Module Type		**YL240P-29b**	
		STC	**NOCT**
Power Output	W	240	174.3
Module efficiency	%	14.7	13.3
Voltage at P_{max}	W	29.5	26.6
Current at P_{max}	A	8.14	6.56
Open-circuit voltage	V	37.5	34.2
Short-circuit current	A	8.65	7.01

Table A1. *Cont.*

Yingli 60 Cell YGE SERIES			
Module Type		**YL240P-29b**	
		STC	**NOCT**
Normal operating cell temperature (NOCT)	°C	46 ± 2	
Temperature coefficient of P_{max}	%/°C	−0.45	
Temperature coefficient of V_{oc}	%/°C	−0.33	
Temperature coefficient of I_{sc}	%/°C	0.06	
Temperature coefficient of V_{mpp}	%/°C	−0.45	
Dimensions(L/W/H)	Mm	1650/990/40	

STC: 1000 W/m^2 irradiance, 25 °C cell temperature, AM1.5 G spectrum according to EN 60904-3; Average relative efficiency reduction of 5% at 200 W/m^2 according to EN 60904-3; NOCT: open-circuit module operation temperature at 800 W/m^2 irradiance, 20 °C ambient temperature, 1 m/s wind speed.

Table A2. Technical characteristics and efficiency ratings of inverters.

Fronius IG Plus 150V-3		
$P_{DC,MAX}$	W	12,770
$I_{DC,MAX}$	A	55.5
$U_{DC,MIN}$	V	230
$U_{DC,START}$	V	260
$U_{DC,R}$	V	370
$U_{DC,MAX}$	V	600
$P_{AC,R}$	W	12,000
$I_{AC,MAX}$	A	17.4
$U_{AC,R}$	V	3-NPE 400/230
Maximum efficiency n_{inv}	%	95.9
n_{inv} at 5% $P_{AC,R}$ (230V/370V/500V)	%	91.8/92.5/91.1
n_{inv} at 10% $P_{AC,R}$ (230V/370V/500V)	%	91.0/94.3/93.2
n_{inv} at 20% $P_{AC,R}$ (230V/370V/500V)	%	94.7/95.1/94.6
n_{inv} at 25% $P_{AC,R}$ (230V/370V/500V)	%	95.1/95.3/94.7
n_{inv} at 30% $P_{AC,R}$ (230V/370V/500V)	%	95.1/95.3/94.9
n_{inv} at 50% $P_{AC,R}$ (230V/370V/500V)	%	95.3/95.9/95.3
n_{inv} at 75% $P_{AC,R}$ (230V/370V/500V)	%	94.7/95.6/95.4
n_{inv} at 100% $P_{AC,R}$ (230V/370V/500V)	%	94.0/95.2/95.1
$P_{DC,MAX}$	W	12,770
$I_{DC,MAX}$	A	55.5
$U_{DC,MIN}$	V	230
$U_{DC,START}$	V	260

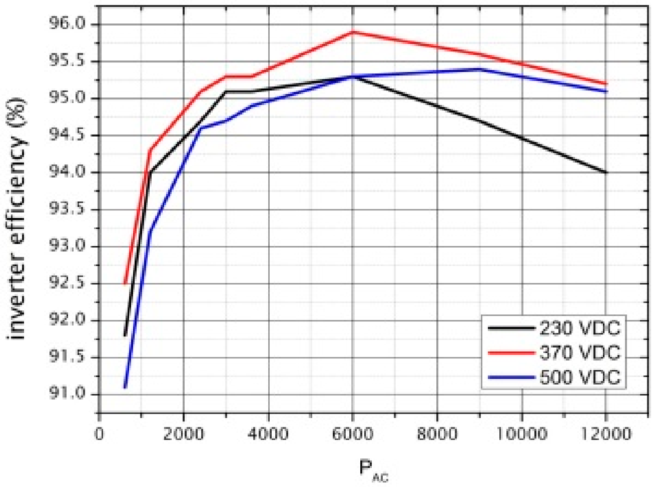

Figure A1. Efficiency curve of inverter with the AC Power for different DC voltages.

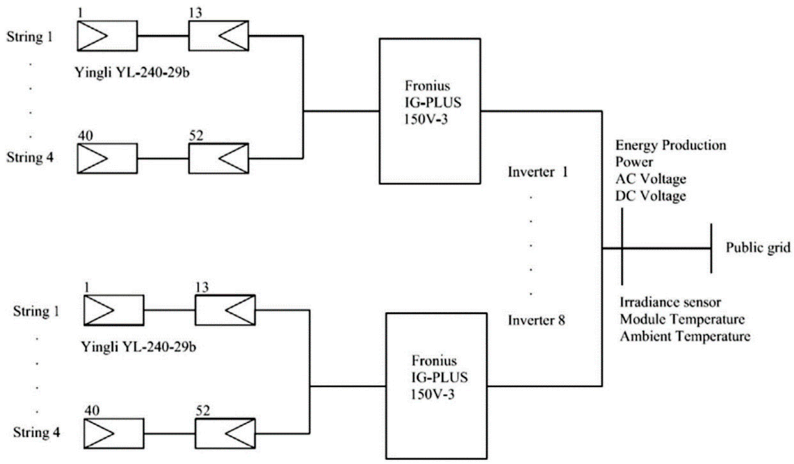

Figure A2. General layout of PV systems.

Table A3. Irradiance sensor characteristics.

Sensor	**Mono-Crystalline Si-Sensor**
Sensor voltage	75 mV at 1000 W/m^2 (exact calibration voltage written on sensor)
Accuracy	±5% (average of a year)
Ambient temperature	−40 °C to +85 °C
Design	Sensor mounted on z-shaped aluminum profile
Dimensions	L × W × H = 55 × 55 × 10 mm
Fronius Product Nr.	43,0001,1189
Temperature Sensor characteristics	
Sensor	PT 100
Measuring Range	−40 °C to +188 °C
Accuracy	±0.8 °C (in the range −40 °C to +100 °C)
Design	Sensor on an adhesive film for measurements on surfaces
Dimensions	32 × 32 mm
Fronius Art. Nr.	43,0001,1190

Appendix B

$$Y_F = \frac{E}{P_{STC}}\left(\frac{kWh}{kW}\right)$$

$$Y_R = \frac{H}{G_{STC}}\left(\frac{kWh}{kW}\right)$$

$$PR = \frac{Y_F}{Y_R}$$

References

1. DAPEEP_SA. Greek Renewable Energy Sources Operator & Issuer of Guarantees of Origin. 2022. Available online: https://www.dapeep.gr/ (accessed on 11 July 2022).
2. Romero, H.F.M.; Rebollo, M.G.; Cardeñoso-Payo, V.; Gómez, V.A.; Plaza, A.R.; Moyo, R.T.; Hernández-Callejo, L. Applications of Artificial Intelligence to Photovoltaic Systems: A Review. *Appl. Sci.* **2022**, *12*, 10056. [CrossRef]
3. Madeti, S.R.; Singh, S.N. A comprehensive study on different types of faults and detection techniques for solar photovoltaic system. *Sol. Energy* **2017**, *158*, 161–185. [CrossRef]
4. Jaen-Cuellar, A.Y.; Elvira-Ortiz, D.A.; Osornio-Rios, R.A.; Antonino-Daviu, J.A. Advances in Fault Condition Monitoring for Solar Photovoltaic and Wind Turbine Energy Generation: A Review. *Energies* **2022**, *15*, 5404. [CrossRef]
5. Kumaradurai, A.; Teekaraman, Y.; Coosemans, T.; Messagie, M. Fault Detection in Photovoltaic Systems Using Machine Learning Algorithms: A Review. In Proceedings of the 2020 8th International Conference on Orange Technology (ICOT), Daegu, Republic of Korea, 18–21 December 2020.
6. Garoudja, E.; Harrou, F.; Sun, Y.; Kara, K.; Chouder, A.; Silvestre, S. Statistical fault detection in photovoltaic systems. *Sol. Energy* **2017**, *150*, 485–499. [CrossRef]
7. Roumpakias Elias, B.F. Stamatelos Anastassios, On-site Inspection of PV Panels, Aided by Infrared Thermography. *Adv. Appl. Sci.* **2016**, *1*, 53–62.
8. Mele, E.; Elias, C.; Ktena, A. Machine Learning Platform for Profiling and Forecasting at Microgrid Level. *Electr. Control Commun. Eng.* **2019**, *15*, 21–29. [CrossRef]
9. Silvestre, S.; Chouder, A.; Karatepe, E. Automatic fault detection in grid connected PV systems. *Sol. Energy* **2013**, *94*, 119–127. [CrossRef]
10. Dhimish, M.; Holmes, V. Fault detection algorithm for grid-connected photovoltaic plants. *Sol. Energy* **2016**, *137*, 236–245. [CrossRef]
11. Hopwood, M.W.; Patel, L.; Gunda, T. Classification of Photovoltaic Failures with Hidden Markov Modeling, an Unsupervised Statistical Approach. *Energies* **2022**, *15*, 5104. [CrossRef]
12. Chine, W.; Mellit, A.; Pavan, A.M.; Kalogirou, S. Fault detection method for grid-connected photovoltaic plants. *Renew. Energy* **2014**, *66*, 99–110. [CrossRef]
13. Huang, M.; Lei, Y.; Li, X.; Gu, J. Damage Identification of Bridge Structures Considering Temperature Variations-Based SVM and MFO. *J. Aerosp. Eng.* **2021**, *34*, 04020113. [CrossRef]
14. Huang, M.; Zhao, W.; Gu, J.; Lei, Y. Damage Identification of a Steel Frame Based on Integration of Time Series and Neural Network under Varying Temperatures. *Adv. Civ. Eng.* **2020**, *2020*, 4284381. [CrossRef]
15. Suresh, V.; Janik, P.; Rezmer, J.; Leonowicz, Z. Forecasting Solar PV Output Using Convolutional Neural Networks with a Sliding Window Algorithm. *Energies* **2020**, *13*, 723. [CrossRef]
16. Fuster-Palop, E.; Vargas-Salgado, C.; Ferri-Revert, J.C.; Payá, J. Performance analysis and modelling of a 50 MW grid-connected photovoltaic plant in Spain after 12 years of operation. *Renew. Sustain. Energy Rev.* **2022**, *170*, 112968. [CrossRef]
17. Hichri, A.; Hajji, M.; Mansouri, M.; Harkat, M.-F.; Kouadri, A.; Nounou, H.; Nounou, M. Fault detection and diagnosis in grid-connected photovoltaic systems. In Proceedings of the 2020 17th International Multi-Conference on Systems, Signals & Devices (SSD), Sfax, Tunisia, 20–23 July 2020.
18. Ammiche, M.; Kouadri, A.; Halabi, L.M.; Guichi, A.; Mekhilef, S. Fault detection in a grid-connected photovoltaic system using adaptive thresholding method. *Sol. Energy* **2018**, *174*, 762–769. [CrossRef]
19. Cui, F.; Tu, Y.; Gao, W. A Photovoltaic System Fault Identification Method Based on Improved Deep Residual Shrinkage Networks. *Energies* **2022**, *15*, 3961. [CrossRef]
20. Voutsinas, S.; Karolidis, D.; Voyiatzis, I.; Samarakou, M. Development of a multi-output feed-forward neural network for fault detection in Photovoltaic Systems. *Energy Rep.* **2022**, *8*, 33–42. [CrossRef]
21. Burbano, R.A.G.; Petrone, G.; Manganiello, P. Early Detection of Photovoltaic Panel Degradation through Artificial Neural Network. *Appl. Sci.* **2021**, *11*, 8943. [CrossRef]
22. Hopwood, M.W.; Stein, J.S.; Braid, J.L.; Seigneur, H.P. Physics-Based Method for Generating Fully Synthetic IV Curve Training Datasets for Machine Learning Classification of PV Failures. *Energies* **2022**, *15*, 5085. [CrossRef]

23. Hichri, A.; Hajji, M.; Mansouri, M.; Abodayeh, K.; Bouzrara, K.; Nounou, H.; Nounou, M. Genetic-Algorithm-Based Neural Network for Fault Detection and Diagnosis: Application to Grid-Connected Photovoltaic Systems. *Sustainability* **2022**, *14*, 10518. [CrossRef]
24. Aljafari, B.; Madeti, S.R.K.; Satpathy, P.R.; Thanikanti, S.B.; Ayodele, B.V. Automatic Monitoring System for Online Module-Level Fault Detection in Grid-Tied Photovoltaic Plants. *Energies* **2022**, *15*, 7789. [CrossRef]
25. Hussain, I.; Khalil, I.U.; Islam, A.; Ahsan, M.U.; Iqbal, T.; Chowdhury, S.; Techato, K.; Ullah, N. Unified Fuzzy Logic Based Approach for Detection and Classification of PV Faults Using I-V Trend Line. *Energies* **2022**, *15*, 5106. [CrossRef]
26. Wang, L.; Lodhi, E.; Yang, P.; Qiu, H.; Rehman, W.U.; Lodhi, Z.; Tamir, T.S.; Khan, M.A. Adaptive Local Mean Decomposition and Multiscale-Fuzzy Entropy-Based Algorithms for the Detection of DC Series Arc Faults in PV Systems. *Energies* **2022**, *15*, 3608. [CrossRef]
27. Omaña, M.; Grossi, M.; Metra, C. Early detection of photovoltaic system inverter faults. *Microelectron. Reliab.* **2022**, *135*, 114594. [CrossRef]
28. Hussain, M.; Dhimish, M.; Titarenko, S.; Mather, P. Artificial neural network based photovoltaic fault detection algorithm integrating two bi-directional input parameters. *Renew. Energy* **2020**, *155*, 1272–1292. [CrossRef]
29. Tkachenko, R.; Izonin, I.; Vitynskyi, P.; Lotoshynska, N.; Pavlyuk, O. Development of the Non-Iterative Supervised Learning Predictor Based on the Ito Decomposition and SGTM Neural-Like Structure for Managing Medical Insurance Costs. *Data* **2018**, *3*, 46. [CrossRef]
30. Álvarez-Tey, G.; García-López, C. Strategy Based on Two Stages for IR Thermographic Inspections of Photovoltaic Plants. *Appl. Sci.* **2022**, *12*, 6331. [CrossRef]
31. Kim, B.; Juan, R.O.S.; Lee, D.-E.; Chen, Z. Importance of Image Enhancement and CDF for Fault Assessment of Photovoltaic Module Using IR Thermal Image. *Appl. Sci.* **2021**, *11*, 8388. [CrossRef]
32. Roumpakias, E.; Stamatelos, T. Prediction of a Grid-Connected Photovoltaic Park’s Output with Artificial Neural Networks Trained by Actual Performance Data. *Appl. Sci.* **2022**, *12*, 6458.
33. Roumpakias, E.; Zogou, O.; Stamatelos, A. Correlation of actual efficiency of photovoltaic panels with air mass. *Renew. Energy* **2015**, *74*, 70–77. [CrossRef]
34. Hagan, M.T.; Demuth, H.B.; Beale, M.H.; De Jesús, O. *Neural Network Design*, 2nd ed.; 2014; ebook; Available online: https://hagan.okstate.edu/NNDesign.pdf (accessed on 11 July 2022).
35. Ahmed, R.; Sreeram, V.; Mishra, Y.; Arif, M. A review and evaluation of the state-of-the-art in PV solar power forecasting: Techniques and optimization. *Renew. Sustain. Energy Rev.* **2020**, *124*, 109792. [CrossRef]
36. El-Baz, W.; Tzscheutschler, P.; Wagner, U. Day-ahead probabilistic PV generation forecast for buildings energy management systems. *Sol. Energy* **2018**, *171*, 478–490. [CrossRef]
37. Wang, F.; Xuan, Z.; Zhen, Z.; Li, K.; Wang, T.; Shi, M. A day-ahead PV power forecasting method based on LSTM-RNN model and time correlation modification under partial daily pattern prediction framework. *Energy Convers. Manag.* **2020**, *212*, 112766. [CrossRef]